Article

Not peer-reviewed version

Giant Aerosol Observations with Cloud Radar: Methodology and Effects

Pilar Gumà-Claramunt *, Fabio Madonna, Aldo Amodeo, Matthias Bauer-Pfundstein, Nikolaos Papagiannopoulos, Marco Rosoldi, Gelsomina Pappalardo

Posted Date: 26 November 2024

doi: 10.20944/preprints202411.1884.v1

Keywords: giant aerosols; cloud radar; aerosols; CCN; GCCN; dust; long-range transport

Article

Giant Aerosol Observations with Cloud Radar: Methodology and Effects

Pilar Gumà-Claramunt [1,*], Fabio Madonna [2], Aldo Amodeo [1], Matthias Bauer-Pfundstein [3], Nikolaos Papagiannopoulos [1], Marco Rosoldi [1] and Gelsomina Pappalardo [1]

[1] Istituto di Metodologie per l'Analisi Ambientale, Consiglio Nazionale delle Ricerche, Potenza, Italy
[2] Università degli Studi di Salerno - Dipartimento di Fisica, Salerno, Italy
[3] METEK GmbH, Elmshorn, Germany
* Correspondence: pilar.gumaclaramunt@cnr.it

Abstract: In this study, an innovative methodology for the identification of giant aerosols using cloud radar is introduced. The methodology makes use of several insects studies and is applied to a 6-year long cloud radar dataset in Potenza, South Italy. 40 giant aerosol events per year were found and are in good agreement with the site's climatological record. A sensitivity study on the effects of the giant aerosols on three atmospheric variables and under different atmospheric stability conditions showed that the presence of giant aerosols: a) increased the Aerosol Optical Depth in all the atmospheric stability conditions, b) decreased the Ångström exponent for the highest and lowest stability conditions and had the opposite effect for the intermediate stability condition, and c) increased the accumulated precipitation in all the atmospheric conditions, specially in the most unstable ones.

Keywords: giant aerosols; cloud radar; aerosols; CCN; GCCN; dust; long-range transport

1. Introduction

Aerosols affect the meteorological and climate system in many ways: by interacting with solar radiation through absorption, scattering and emission; by acting as Cloud Condensation Nuclei (CCN) and Ice Nuclei (IN), upon which cloud droplets and ice crystals form; and by carrying nutrients to oligotrophic ecosystems, such as oceans. Moreover, they also have a large impact on human health by causing or enhancing respiratory, cardiovascular, infectious, and allergic diseases [1] and can affect air transport, as happened during the spring of 2010, when the Eyjafjallajökull volcano eruption in Iceland caused an enormous disruption to air traffic across western and northern Europe [2].

Aerosol sizes range from few nanometers to tenths of micrometers, can be of natural or anthropogenic origin and have different compositions. The aerosols effects and importance depend on their concentration and characteristics. Cloud Condensation Nuclei (CCN) and Ice Nuclei (IN) particles determine to a large extent cloud microstructure and, consequently, cloud albedo and the dynamic response of clouds to aerosol-induced changes to precipitation [3]. The aerosol size distribution, and in particular the availability of Giant CCN (GCCN), has a major impact on cloud development and rain formation [4]. By acting as GCCN, giant ($> 1\ \mu m$ radius) and ultragiant particles ($> 2.5\ \mu m$ radius), can determine the concentration of the initial cloud droplets, the clouds albedo and lifetime, and the precipitation formation, expediting specially warm rain processes [5,6]. In addition, depending on their composition, they can also act as IN. Mineral dust, for instance, is an efficient IN [7], being the bigger particles with larger surface areas the first to nucleate [8]. In a cloud seeding experiment by Ghate *et al.* [9], it was found that although the giant nuclei introduced into a cloud were only a small fraction of the total aerosols, they dominated the cloud response. Besides, during a field campaign in Barbados (BACEX, March-April 2010), it was found that during dusty periods, aerosol concentrations increased substantially in the size range between 0.5 and 10 μm (diameter) [10], which might have an important impact on aerosol–cloud–precipitation interactions because the most effective GCCN size lies within this range [10–12]. Nevertheless, other studies have reported a minor or no effect of GCCN on the initiation of rain in warm convective clouds [i.e. 13–15].

Although lidar and photometer are the main instruments in aerosol monitoring, they do not account for giant and ultragiant aerosols bigger than a a few microns. Specifically, given the wavelength

 doi:10.20944/preprints202411.1884.v1

used by the aerosol lidars, the retrieval of microphysical properties is limited to 10 μm [16] whereas, similarly, sun photometers have a 15 μm cutoff [17]. Giant dust particles have been observed at great distances from their source: van der Does *et al.* [18], for example, reported observations of individual giant Saharan dust particles of up to 450 μm in diameter sampled in air over the Atlantic Ocean at 2400 and 3500 km from the west African coast. In Europe, giant dust particles were found > 4000 km from their Saharan source by using sediment traps [19], and dust particles up to 300 μm in diameter were sampled during aircraft campaigns over north-western Africa [20]. Therefore, the complete distribution and impact in the atmosphere and climate of these particles is not well known, and the aerosol transport models largely underestimate them [21]. Conversely, cloud radars can complement the existing gap and detect giant and ultragiant particles, and even though we have not found in literature dust giant particles observations made by cloud radars at a long distance from the source, a Ka-band cloud radar detected volcanic ultragiant particles far from the source [22], with observed values of radar reflectivity that are consistent with a particle effective radius larger than $50 - 75$ μm [23].

In this work, we present an innovative methodology for identifying giant aerosols using cloud radar observations, which is developed on the basis of entomology studies to discriminate the contribution of insects from aerosol in the low troposphere. The instrumentation and the methodology are presented in Section 2. In Sect. 3, the methodology is applied to 6 years of continuous measurements, where the effects of giant aerosols are studied by comparing different atmospheric variables under different atmospheric stability conditions. The paper closes with conclusions and suggestions for further applications and improvements.

2. Materials and Methods

2.1. Instrumentation

This study has been carried out at the CNR-IMAA Atmospheric Observatory (CIAO, www.ciao.imaa.cnr.it), located in Tito Scalo, Potenza, Southern Italy, on the Apennine mountains (40.60°N, 15.72°E, 760 m *a.s.l.*), less than 150 km from the West, South and East coasts [24]. The site is in a plain surrounded by low mountains (< 1300 m *a.s.l.*) and has a coastal Mediterranean climate (Köppen type Csb), characterized by dry, warm summers and wet, cold winters. The site is of particular interest for studying aerosol properties because it is affected by a quite large number of Saharan dust intrusions per year [25] and it is located 300 km far from the Etna volcano [26].

The main instrument used in this study is a Ka-band Doppler radar. Ancillary data acquired by other instruments, such as a microwave radiometer and a weather station, as well as the output of a Numerical Weather Prediction (NWP) model are also used to achieve the purposes of this study.

A millimetre-wavelength cloud radar (MIRA36) from METEK GmbH is operating at CIAO since March 2009. It is a mono static magnetron-based pulsed Ka-Band Doppler radar operating at 8.45 mm wavelength; it has a sensitivity of -55 dBZ at 1 km and -40.3 dBZ at 5 km [24]. According to its configuration, the time and range resolution are 10 *seconds* and 30 *meters* respectively. Linearly polarized signal is transmitted, while co- and cross polarized signals are received simultaneously to detect Doppler spectra and Linear Depolarization Ratio (LDR). Out of the Doppler spectra, the Signal-to-Noise Ratio (SNR), the Doppler velocity (VEL), the peak width (RMS) and the equivalent reflectivity (Z) are retrieved.

Measurements from three additional ground-based remote sensing instruments, a microwave radiometer profiler (MWR), a ceilometer and a sun photometer, are used. The MWR (MP3014 from Radiometrics) measures the sky Brightness Temperature (BT) at 12 frequencies; the inversion of this quantity provides temperature, humidity and cloud liquid water profiles up to 10 km as well as an estimation of the Integrated Water Vapour (IWV) and the cloud Liquid Water Path (LWP) [24]. The ceilometer (CT25K from VAISALA) is continuously measuring the cloud-base height and the signal backscattered by atmospheric particles at 905 nm up to 7.5 km [24]. The sun photometer (CE-318 from

 doi:10.20944/preprints202411.1884.v1

CIMEL) measures the direct solar irradiance and sky radiance at the Earth's surface. It is operational within the AERosol RObotic NETwork (AERONET), performs columnar measurements and one of its main products is the multi-wavelength Aerosol Optical Depth (AOD), that can be used to estimate the aerosol size distribution [24].

In situ measurements are used as well: standard surface variables (pressure, temperature, humidity and wind) are routinely monitored using the MILOS520 Automatic Weather Station [24], while radiosounding observations of temperature, pressure, humidity and winds are considered when available.

Moreover, data outputs from the European Centre for Medium-Range Weather Forecasts (ECMWF) Integrated Forecast System Model, with an horizontal resolution of 39 km, 60 vertical levels and a forecast temporal range between 12 and 35 *hours* are also used in this study.

2.2. Cloud Radar Aerosols Observation

In this study, giant aerosols are observed by cloud radar in a systematic way and for a long time period. To this purpose, it is preliminarily needed to determine the sizes of the atmospheric particles that can be detected by the cloud radar according to its sensitivity. Afterwards, a novel methodology has been developed to detect these particles by using the MIRA36 cloud radar.

2.2.1. Sensitivity Limits

The cloud radar operating wavelength determines the atmospheric constituents it can detect. Since airborne particles are smaller than cloud droplets or rain drops, it is important to quantify the radar capability to detect aerosols with different particle effective radii. With this purpose, the T-matrix method for randomly oriented, rotationally symmetric scatterers [27] has been used to compute the extinction and scattering efficiency and the Müller matrix of aerosols at the cloud radar wavelength. These calculations necessitate the a priori inference of the aerosol complex refractive index.

As we were unable to find the complex refractive index for dust at the cloud radar wavelength (8.45 mm), we searched for the refractive indices of dust reported in literature at other wavelengths. In Zhang *et al.* [28], they presented a recollection of refractive indexes for dust with different mineralogical compositions between 0.2 and 50 μm, which shows that the refractive index changes significantly between different wavelengths. At 800 nm, the refractive index real part ranges between 1.4 and 2.9, whilst the imaginary part falls between $2\ 10^{-6}$ and 0.015. At 50 μm, the ranges are $1.8 - 5.9$ and $0.02 - 1.5$ for the real and imaginary parts respectively. In the study of Weinzierl *et al.* [29], they presented the refractive index of volcanic aerosols and dust between 350 and 800 nm. At 800 nm, the same wavelength that we selected from [28], the refractive index for dust was of $1.544 + 0.0005i$, and for volcanic of $1.551 + 0.078i$. Given the high variability of the complex refractive index that we see at different wavelengths, and that the values for dust and volcanic particles are relatively similar at the same wavelength (800 nm), we decided to use the complex refractive index found by Adams *et al.* [30] for volcanic particles at the radar operating frequency (35.5 GHz): $2.45 + 0.43i$.

The equivalent reflectivity (Z) and Linear Depolarization Ratio (LDR) can be computed from the elements of the Müller matrix. Figure 1 reports the estimated theoretical reflectivity at 8.45 mm for spherical particles depending on their size and number concentration. The reflectivity is increasing together with the particle radius and the number concentration; the highest increase is associated to the particle size. As previously mentioned, according to the manufacturer the radar sensitivity threshold is $-55\ dB$ at 1 km at a time resolution of 10 *seconds* and averaging 200 spectra; reflectivity values above this value are highlighted using white horizontal lines. This means that the particles with the corresponding effective radius and number of particles can be detected by the MIRA36 cloud radar. A particle of 1 μm radius, for example, cannot be measured if its number concentration is below 10 cm^{-3}. A 2 μm radius particle, instead, will be detected if the number concentration is higher than 0.2 cm^{-3}. And finally, all particles with a radius of 5 μm or bigger will be detected if their number concentration is as low as 0.001 cm^{-3}. These values are in line with giant aerosol observations in the atmosphere,

 doi:10.20944/preprints202411.1884.v1

such as Exton *et al.* [31], who found total particle concentrations of a few-per-centimeter cubed in the range $1 - 23.5\ \mu m$, and of about $0.1 - 0.5\ cm^{-3}$ in the range $5 - 150\ \mu m$, and with the measurements performed during the First Aerosol Characterization Experiment (ACE-1), that measured particles with dry radii on the order of 6 to 12 μm in concentrations between 10^{-4} and $10^{-2}\ cm^{-3}$ [5].

Therefore, given the radar sensitivity, the T-Matrix scattering calculations, and the aerosols size and number concentration in the atmosphere, we can affirm that the cloud radar is sensitive to giant and ultragiant aerosols.

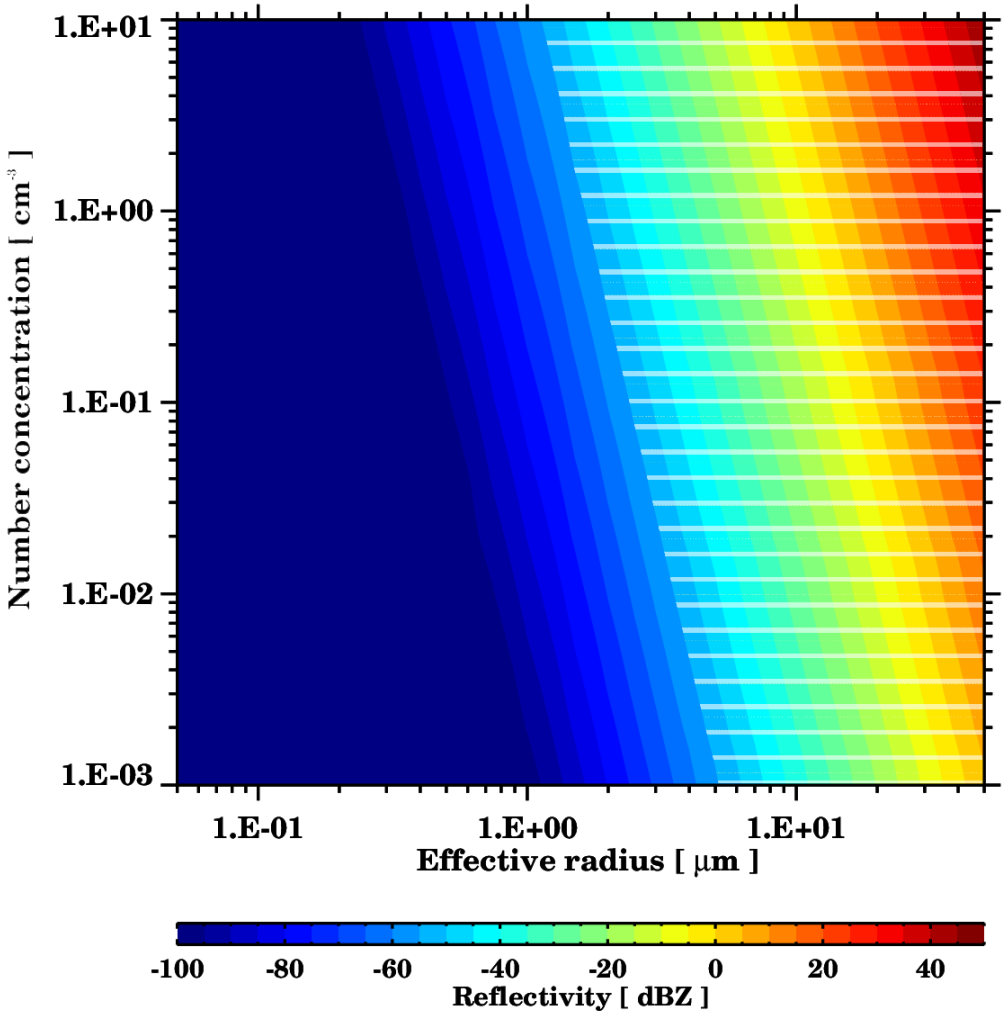

Figure 1. Reflectivity calculations from the output of Mishchenko's T-matrix scattering code depending on the particle effective radius and the number of particles. These values correspond to spherical particles at a wavelength of 8.45 mm, to a complex refractive index of $2.40 + 0.40i$, and to a scattering angle of 180°. The white horizontal lines highlight reflectivities over $-55\ dB$, the radar sensitivity threshold at 1 km.

2.2.2. Detection Methodology

The microwave radiation emitted by the radar probes the atmospheric vertical structure, and receives echoes caused by different kinds of scatterers (hereinafter targets). The target discrimination is essential for interpreting the cloud radar observations, and in many cases this operation can be accomplished by using the different Doppler velocities and LDR. In the cloud radar MIRA36 algorithms, following the noise (the so-called clutter) removal, the targets are classified into clouds, rain and plankton; being the latter the radar term used to describe non-hydrometeor targets (i.e.

 doi:10.20944/preprints202411.1884.v1

insects). Ka and W-band cloud radars (35 and 94 GHz respectively) detect almost exclusively insect targets on warm cloudless days [32,33]. Indeed, radar has been applied to the study of insects for more than 40 years. Since wind-borne insect migration occurs on a colossal scale, far exceeding (at least in numerical terms) the migratory flux of birds [34] and giant and ultragiant volcanic aerosols can be detected by Ka-band radars [22,23,35,36], it can be assumed that the non-hydrometeor (plankton) echoes consist of insect and aerosol returns only. Therefore, a strategy has been developed based on insects characteristics and behaviour to detect and subtract them from the radar signals, keeping the aerosol returns only.

The first of the insects characteristics that has to be taken into account is their vertical evolution throughout the day. The depth of the insect layer follows the diurnal variation of the Atmospheric Boundary Layer (ABL) with a minimum during night-time, sharply increases in the morning, and reaches a maximum in the afternoon. According to this daily evolution, represented in Figure 2, crepuscular, diurnal and nocturnal insects can be identified with almost no overlap between them. Crepuscular species take-off during the morning twilight period, with small numbers and a generally short-lived flight, although occasionally continue for some time and day-time layers are reported [34]. Day-flying migrants take off from mid-morning onward, as atmospheric convection develops, and generally descend in the late afternoon; occasionally, small numbers of day-flying species continue their migration into the night [34]. Nocturnal species typically have a mass take-off at dusk and fly throughout the night following the stratification of the nocturnal BL [37–41]. Therefore, they tend to concentrate into layers of shallow depth but broad horizontal extent [42–45].

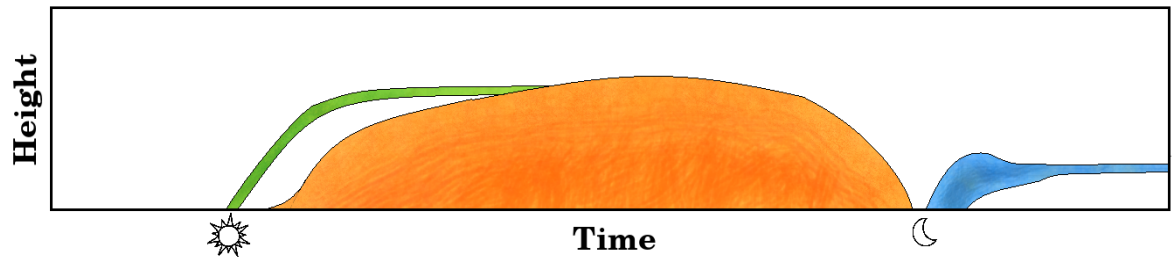

Figure 2. Insect daily schematic evolution, in three distinguished groups: crepuscular (green), diurnal (orange) and nocturnal (blue). The height reached by the insects depends on the geographical location and meteorological conditions. Elaborated based on Chapman *et al.* [34,37], Drake [42], Drake and Farrow [43], Gatehouse [44], Reynolds *et al.* [38,39,45] and Wood *et al.* [40,41].

Typically, insects size range is of the order of millimeters, whereas aerosols size range after atmospheric transport can reach up to a few hundred microns. Considering that the radar reflectivity is proportional to the sixth power of the diameter of the scatterers, aerosols are only detectable in range gates free of insects. Therefore, only the lofted layers relative to the areas where the insects fly are searched for and further processed.

Figure 3 illustrates the approach that has been developed with this purpose. First, according to the cloud radar original classification [46], the plankton (non-hydrometeor) layers are looked for. Due to the speckled nature of the cloud radar images, it was established that the lofted layers should have 600 pixels at least (10 samples in height $\times$ 60 samples in time), which corresponds to a 300 m thick layer that lasts for 10 min. Second, the misclassification of the outer cloud and rain pixels into the plankton category that is frequently done by the original cloud radar classification algorithm needs to be overcome. With this purpose, the cloud and rain areas are expanded 2 min in time and 120 m in range to create a cloud mask. This mask includes the clouds and rain regions, including their outer originally misclassified pixels. Third, the cloud base height detected by the ceilometer is also included into the mask in order to avoid inserting misclassified clouds into the process. Finally, after applying the cloud mask, the remaining layers are classified into lofted or not lofted depending on their minimum height.

 doi:10.20944/preprints202411.1884.v1

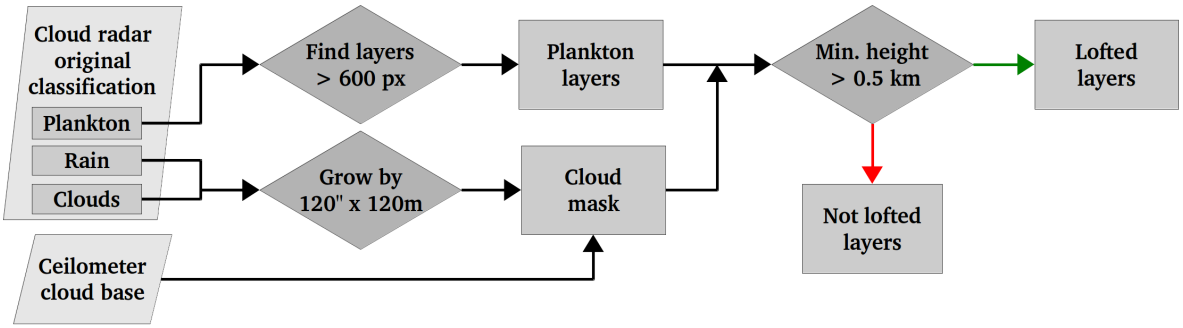

Figure 3. Methodology adopted for the identification of non-hydrometeor targets lofted layers. The green arrow indicates the condition is fulfilled, the red one that it is not.

After the identification of the plankton lofted layers via the process that we just described, a series of tests based on the insect behaviour in the atmosphere are carried out to distinguish between the aerosol and insect layers. The different criteria are based on entomology studies and consider atmospheric variables such as the temperature and the wind. The key features of insects layers are explained next.

Two aspects of the insects relation with temperature were considered: (a) the ceiling (maximum height) of the insect layer can be approximated by the $10°C$ isotherm in most cases, even though there is a tendency of insects to tolerate lower temperatures after prolonged periods with temperatures lower than average [47]; and (b) the insect layers during night-time are frequently located near the inversion top height [38].

Regarding the insects behaviour with respect to the wind, it was found that (a) they do not fly at a wind speed on the Beaufort wind force scale higher than 5 close to the ground [48], which corresponds to a mean wind speed of 10 $m\ s^{-1}$; and that (b) the aerosol layers tend to follow the 3D wind vector, while insects usually have a more random behaviour.

Finally, concerning the relation of the insects with the convection, the ABL and the height, it is known that (a) insects tend to be concentrated in plumes of rising air [49]; that (b) there are usually many more insects within the convective ABL than above it [50]; and that (c) migrating insects typically fly at high altitudes, sometimes as high as 2 or 3 km above the ground [44].

Figure 4 illustrates the developed methodology based on entomology criteria outlined above. In order to perform the following screening steps, ancillary information is required. Temperature and wind profiles from radiosondes are used, if available, within a temporal difference of 2 h (we assume that within this time interval the measured profiles are still representative of the actual conditions). In any other case, profiles provided by the MWR and the ECMWF model are used for temperature and wind respectively.

In the first step, the layers that have more than 60% upward Doppler velocities are classified as insects. If not, then it is a possible aerosol layer and goes through the second screening step. In the second step, which is only applied during night, the layer location relative to the temperature inversion height is used as the screening metric. If more than 10% of the layer is located within 500 m higher or lower of the temperature inversion height, it is classified as an insect layer. If not, it goes ahead in the classification procedure. In the third screening step, four tests are applied:

- is the temperature of more than 90% of the points below $0°C$?
- are more than 90% of the layer pixels located above 3 km?
- is the corresponding horizontal wind speed of at least 90% of the layer pixels over 10 $m\ s^{-1}$?
- is the difference of angle between the layer and the isotachs time-height cross section orientation lower than 30°?

The layer that meets at least one of these conditions is classified as aerosol. If not, it falls into the insect category.

 doi:10.20944/preprints202411.1884.v1

Since radar measurements alone cannot provide unique information on whether giant aerosols are embedded in the insect layers due to their highly differing sizes, it is necessary to check independent measurements to further scrutinise the results obtained from the cloud radar. For this reason, the insect layers are submitted to an additional screening criterion. The size distribution retrievals from the AERONET sun photometer during the insect layer are averaged. Then, if the effective radius of the coarse mode is smaller than 2.5 μm it is considered that it is an insect layer, whilst otherwise we assume that is a layer of insects with embedded giant aerosols. This criterion can only be applied during day-time, when the sun photometer is operating. During night-time, the atmospheric conditions are generally more stable and, in addition, the cases occurring in this period are checked for the temperature inversion.

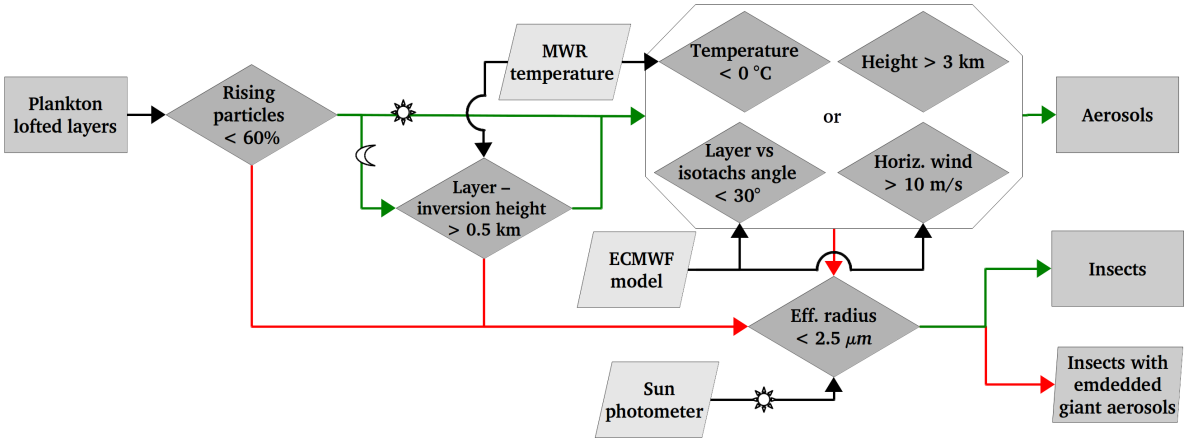

Figure 4. Methodology used for the creation of the aerosol-insect dataset, applying tests based on entomology studies. Green arrows indicate the condition is fulfilled, and red arrows that it is not.

3. Results

3.1. Giant Aerosols Dataset

The described methodology was applied to all the cloud radar observations in Potenza within the period of March 2009 - June 2015, resulting in the identification of 328 aerosol layers, 684 insect layers and 18 insect layers with embedded giant aerosols. The selection of this time interval was based on having the longest data records at the station without gaps due to maintenance, tests and temporarily instrument shut-down.

Table 1 shows the day/night distribution of the identified layers.

Table 1. Aerosols, insects and insects with embedded giant aerosol lofted layers dataset (March 2009 - June 2015). Between parentheses is the percentage of layers of the total. Note that some layers have a long duration and occur both during day- and night-time.

Layers	Aerosols	Insects	Insects with embedded giant aerosol
Day-time	175 (16.8%)	270 (26.0%)	18 (1.7%)
Night-time	155 (14.9%)	421 (40.5%)	0 (0.0%)
Total	328 (31.8%)	684 (66.5%)	18 (1.7%)

The number of aerosol layers during day and night is very similar, while the number of insect layers during night is much higher than during day. This agrees with the entomology studies description of the insects behaviour: they mainly fly within the ABL during the day and follow the stratification of the ABL during the night. Nevertheless, this could also be caused by one of the steps in the screening

 doi:10.20944/preprints202411.1884.v1

procedure, in which the temperature inversion height is compared to the height of the aerosol/insect layer. The information from the sun photometer, used to detect embedded giant aerosol layers, was available for the 48.3% of the total insect cases, and it was found that the 12.9% of the insect layers to which this criterion could be applied contained giant aerosols. Henceforth, only the aerosol and insect layers without embedded giant aerosols will be considered in order to compare the two targets.

The frequency distributions of the reflectivity (Z) and LDR for aerosols and insects are shown in Figures 5 and 6. The reflectivity distribution (Figure 5) is very similar for both targets. Nonetheless, some small differences are observed: low reflectivity values are observed more frequently for insects, while aerosols reach higher values. The LDR distribution (Figure 6) is bimodal for the aerosols and unimodal for the insects, being the low values more common for the aerosols. This indicates that the SNR difference between the co- and the cross-channel is, in general, higher for aerosols. This effect might be due to the effective irregularities of the two targets; for aerosols, non-zero LDR values indicate the presence of non-spherical aerosols and can be highly sensitive to particle shapes and sizes [51].

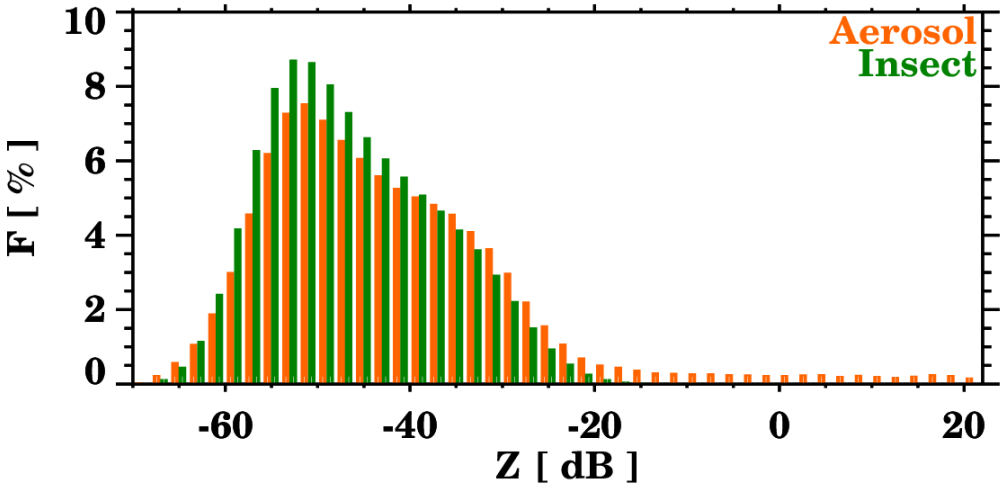

Figure 5. Frequency distribution of reflectivity for all the aerosols (in orange) and insect cases (in green).

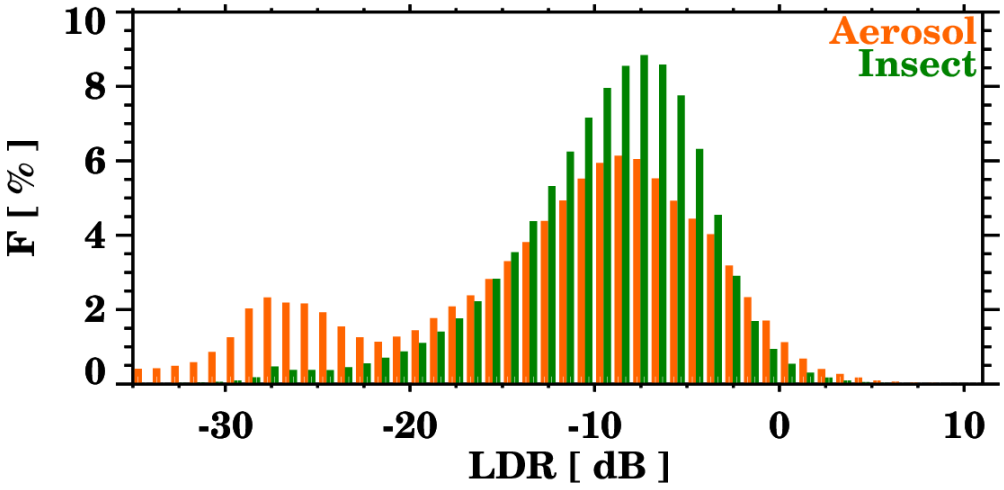

Figure 6. Frequency distribution of LDR for all the aerosols (in orange, bi-modal distribution) and insect cases (in green, mono-modal distribution).

 doi:10.20944/preprints202411.1884.v1

In Figure 7 the occurrence of the aerosol layers throughout the year is presented. The maximum number of aerosol layers observed occurs during summer (July and August), whilst the minimum occurs during winter. The number of aerosol cases decrease gradually from summer to winter. From winter to summer, there is a gradual increase of the aerosol layers detected, with the exception of a relative maximum in April. These features are in accordance to climatological studies of the site [25,52]. Most likely, the peak during spring is caused by pollen and dust and the one during summer by dust.

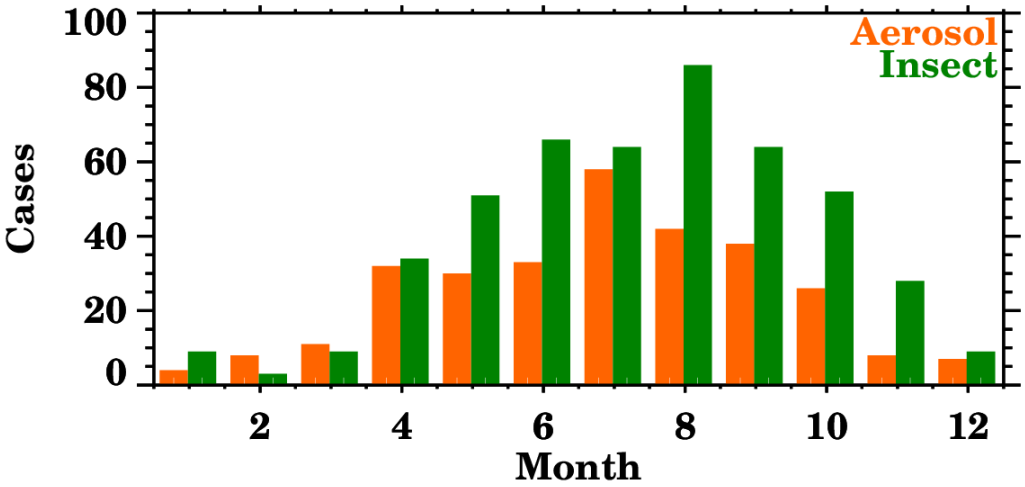

Figure 7. Number of aerosol (in orange) and insect layers (in green) per month. As the total number of cases is presented instead of the frequency distribution, the total number of insect layers is much higher than the number of aerosol layers.

The annual evolution of Aerosol Optical Depth (AOD) retrieved by the AERONET sun photometer is presented in Figure 8 together with the normalized frequency distribution of giant aerosol cases. The AOD curves and the distribution of the giant aerosol observations yield a good agreement: the highest AOD values are observed during the months in which more giant aerosol cases occur. The enhanced AOD values during spring and summer agree with the annual cycle of dust outbreaks [25,53], suggesting the presence of coarse mode aerosols over Potenza.

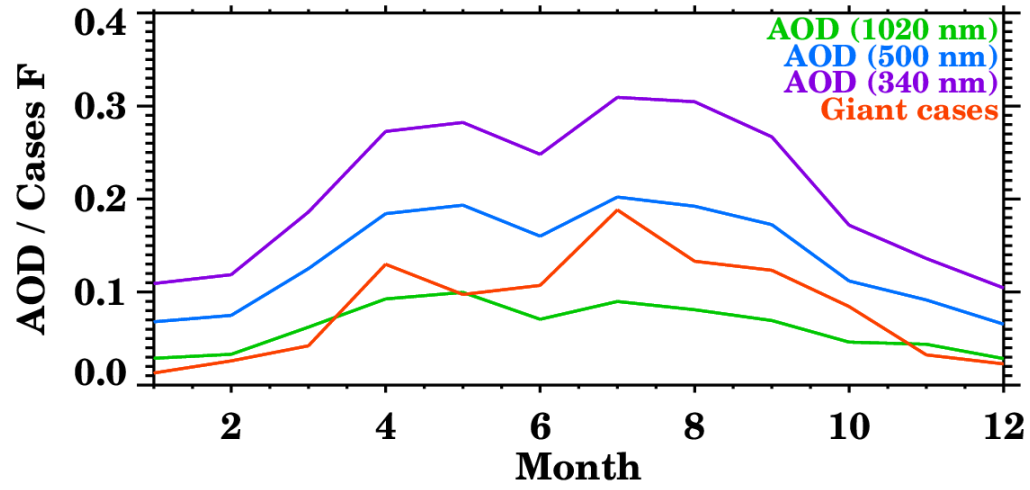

Figure 8. Frequency distribution of giant aerosols cases (orange line) as observed by the cloud radar together with AOD measured by AERONET at 340, 500 and 1020 *nm*.

 doi:10.20944/preprints202411.1884.v1

Concerning the layers vertical distribution (Figure 9), aerosols are usually located at higher altitudes compared to insects. This is caused by the preference of insects to stay within the ABL. Figure 10 shows the distribution of the percentage of rising particles of the layers: most of the times, the aerosol layers have a vertical velocity close to zero (of the total number of particles in each layer, between the 40 and 60% have ascending velocities), and in some cases most of the particles are falling (lower percentage of rising particles within each layer). This characteristic helps to distinguish these layers from the insect ones, as insects tend to follow the upward motion of the air parcels.

The fact that there are no aerosol layers that contain more than 60% of rising particles is a consequence of our algorithm for the giant aerosols detection.

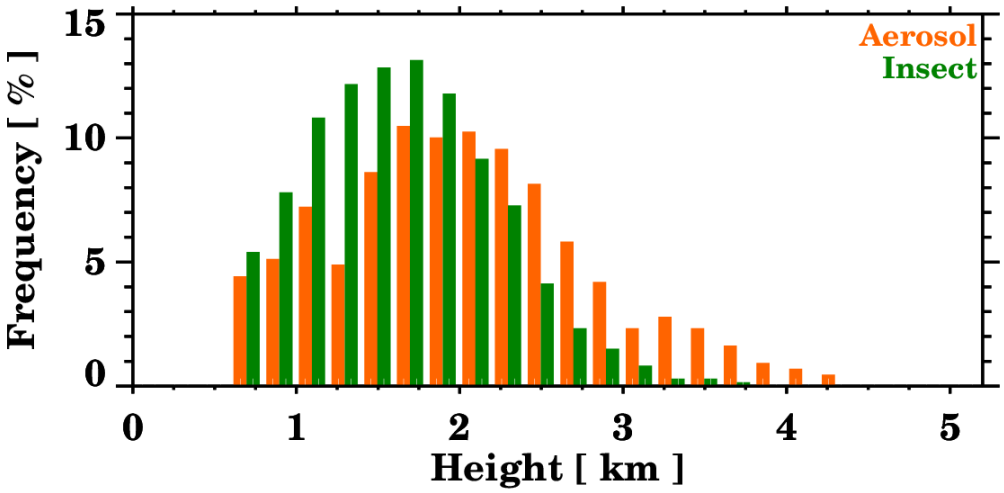

Figure 9. Frequency distribution of the height location of the insect (in green) and aerosol layers (in orange).

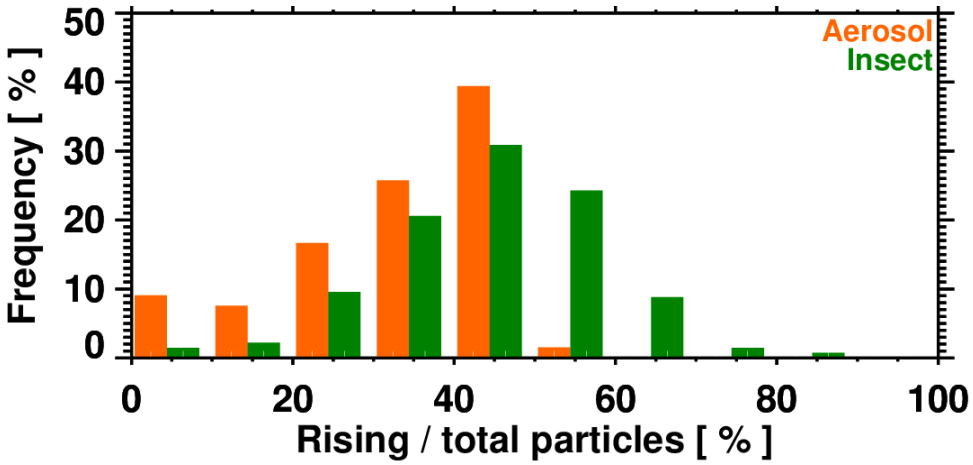

Figure 10. Frequency distribution of the proportion of particles with upwards velocity within the insect (in green) and aerosol layers (in orange).

3.2. Giant Aerosols Effects

The ultimate goal of observing giant aerosols is to study their effects to get a better understanding of the processes that they are involved in and their importance for meteorology and climate. To this purpose, we have made a comparison of the values of some atmospheric variables depending on whether giant aerosols were observed or not. Control cases are days in which giant aerosols were not

 doi:10.20944/preprints202411.1884.v1

observed by the cloud radar. The variables that have been considered are the Aerosol Optical Depth (AOD), the Ångström exponent and the accumulated precipitation.

In order to study the giant aerosols effects on these variables, it is necessary to account for the diurnal cycle and the meteorological situation.

The diurnal cycle is an important factor in the development of the ABL, the convective activity, and the formation of clouds and rain, and therefore needs to be taken into account. To account for it, a time period of the day needs to be selected and used for all the cases. The time interval selected here is from 13:00 to 14:00 local time (LT), selected on the basis of Koren *et al.* [54], who made a study on the aerosol-induced intensification of rain from the tropics to the mid-latitudes and set the time for his study at 13:30 LT.

The meteorological situation is assessed by sorting the data into cases with different pressure vertical velocities (ω) of the upper troposphere (400 hPa), as in [54]. Negative pressure vertical velocities indicate a net upward air motion, related with more developed clouds and higher rain rates (R). Positive pressure vertical velocities indicate net downward motion, related to fair weather. According to the pressure vertical velocities from the ECMWF model, three stability levels were defined for this study:

- Stability condition 1: $\omega \leq -0.001\ Pa\ s^{-1}$
- Stability condition 2: $-0.001 < \omega \leq 0.001\ Pa\ s^{-1}$
- Stability condition 3: $\omega > 0.001\ Pa\ s^{-1}$

The use of the vertical velocity measured by the cloud radar in the higher troposphere was considered to establish the different atmospheric stability conditions, but we disregarded it because it could be affected by cloud vertical dynamics (i.e. the ice cloud targets normally show significant terminal falling velocities), because imperfect pointing of the vertical beam can generate an offset that is large compared to the synoptic ω-values, and because it was not always available (i.e. clouds not present).

The selection of control cases (not giant aerosol observations) is based on the size distribution retrievals from AERONET and for the same time interval (13:00 – 14:00 LT). Therefore, days in which there were no giant aerosols cloud radar observations and the effective radius of the coarse mode is lower than 2.5 μm are flagged as control cases. This retrieval was available for 212 of the 2107 considered days (March 2009 - June 2015), and the screening filter was met for 173 cases.

The giant observations are selected from the cloud radar giant aerosols dataset. The cases are selected if they occurred less than 4 h before or after the predefined time interval, limiting, thus, the cases to a fully developed ABL. From the initial 328 cases of giant aerosol observations, 150 passed this specific filter.

After the selection of the two datasets (giant aerosols and control) and their classification according to the meteorological situation, 150 giant aerosol and 159 control cases were found. Table 2 reports the number of cases classified according to their atmospheric stability category.

Table 2. Number of giant and not giant cases for the initial conditions (giant cases within the time interval defined and not giant cases with a coarse mode effective radius $< 2.5\ \mu m$) and with available pressure vertical velocity (ω) data. The stability types defined are: 1 ($\omega \leq -0.001\ Pa\ s^{-1}$), 2 ($-0.001 < \omega \leq 0.001\ Pa\ s^{-1}$) and 3 ($\omega > 0.001\ Pa\ s^{-1}$).

Stability condition	Dataset	
	Giant	Control
1	33	47
2	88	70
3	29	42
Total	150	159

 doi:10.20944/preprints202411.1884.v1

In the following, we assess the giant aerosol effects on three independent parameters: the Aerosol Optical Depth (AOD), the Ångström exponent and the accumulated precipitation.

3.2.1. Aerosol Optical Depth

The mean AOD during the control and giant aerosol events at 340, 500 and 1020 *nm* is presented in Figure 11 and summarized in Table 3. For all the atmospheric conditions and all the wavelengths we noted an increase of the mean AOD values when giant aerosol were observed. This increase ranged from 0.004 to 0.164 in absolute values, and from 6% to 90% in relative terms.

The highest differences were found for Conditions 1 and 3, whereas for Condition 2 the effect was less pronounced. At 340 *nm*, for example, the AOD went from 0.187 to 0.297 for Condition 1 (0.11 increase, 59%), and from 0.183 to 0.347 for Condition 3 (0.164 increase, 90%). These higher increases during the most stable and unstable atmospheric conditions can be linked to the meteorological situation affecting the site at the time of the observations. Figure 12 presents a schematic of a theoretical meteorological situation affecting the site for the stability conditions 1 and 3. The site is affected by low pressures in Condition 1 (blue) and by high pressures in Condition 3 (in red). According to the seasonality of the giant aerosols observations (Figure 7), it is likely that most particles observed over Potenza originate in the Sahara desert. Therefore, the higher increases of AOD caused by giant aerosols can be related to the flow of desert dust particles towards the site, both in low and high pressure conditions. The dust particles reaching the observational site, though, will most likely have different characteristics, as under low pressure conditions the particles will be fresher, whilst under high pressure conditions they will be more aged due to a longer range transport.

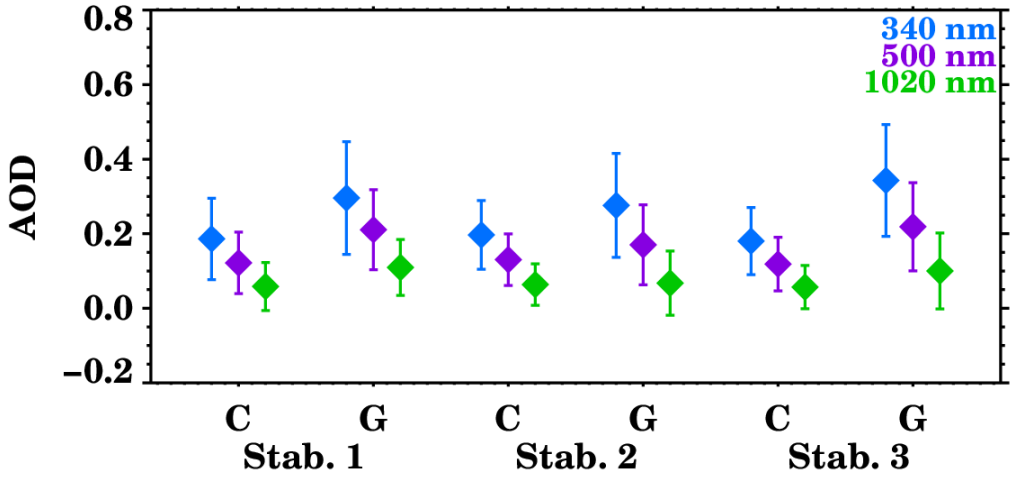

Figure 11. Mean Aerosol Optical Depth (AOD) values at 340, 500, and 1020 *nm* during control and giant aerosol cases according to the atmospheric stability. The error bars correspond to the standard deviation. "C" stands for control cases, "G" for giant aerosols observations, and "Stab." for atmospheric stability condition, where "1" has the lower stability and "3" the highest.

 doi:10.20944/preprints202411.1884.v1

Table 3. Mean Aerosol Optical Depth (AOD) values during control and giant aerosol cases according to the atmospheric stability, where "1" has the lower stability and "3" the highest. The values after the ± sign correspond to the standard deviation.

Wavelength [nm]	Stability condition 1		Stability condition 2		Stability condition 3	
	Control	Giant	Control	Giant	Control	Giant
340	0.187 ± 0.103	0.297 ± 0.157	0.191 ± 0.085	0.267 ± 0.129	0.183 ± 0.090	0.347 ± 0.155
500	0.120 ± 0.082	0.208 ± 0.101	0.132 ± 0.069	0.173 ± 0.113	0.121 ± 0.069	0.223 ± 0.122
1020	0.055 ± 0.070	0.103 ± 0.066	0.065 ± 0.058	0.069 ± 0.088	0.058 ± 0.059	0.102 ± 0.103

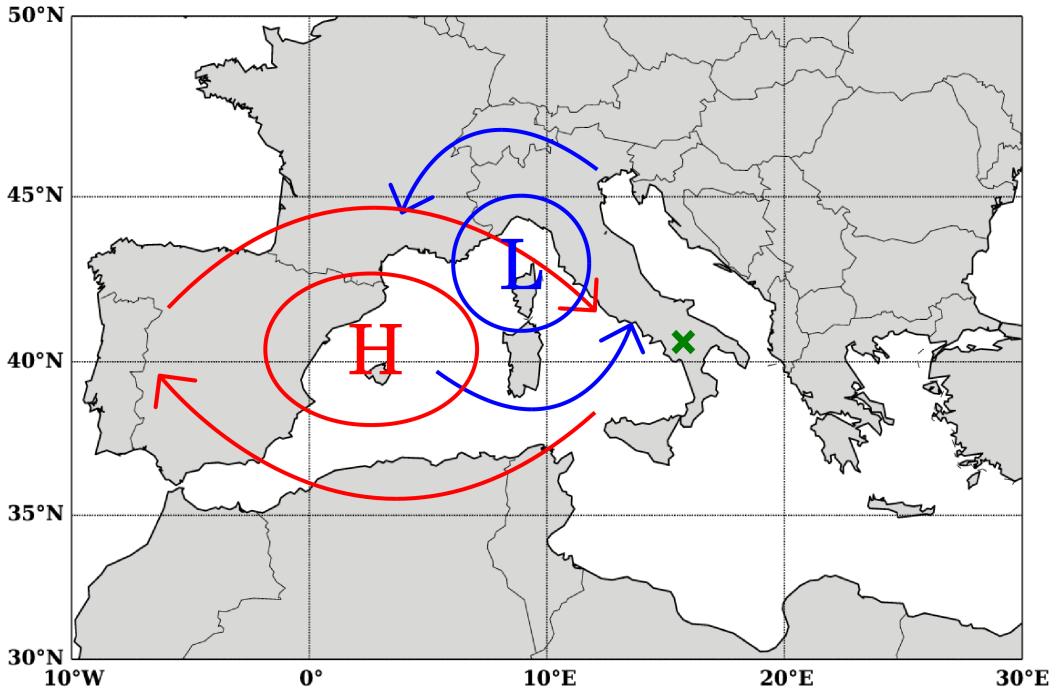

Figure 12. Scheme of the synoptic situation corresponding to the atmospheric stability conditions "1" (blue) and "3" (red). "L" stands for a low pressure system (cyclone) and "H" for a high pressure system (anticyclone). The green cross indicates the observatory location.

3.2.2. Ångström Exponent

The Ångström exponent, which is an aerosol size-related parameter, is also affected by the presence of giant aerosols. Figure 13 represents the change at three wavelength pairs (380 − 500 nm, 440 − 675 nm and 500 − 870 nm) for control and giant observations, classified according to the atmospheric stability condition. The values are reported in Table 4. In this case, an Ångström exponent decrease is observed for all the pairs of wavelengths for the lower atmospheric stability (Stab. 1): around −30% for all of them. The highest difference was observed for the 440 − 675 nm pair, where the Ångström exponent decreased from 1.5 to 1.06 (−0.44 change). The opposite behaviour is observed for the neutral atmospheric stability (Stab. 2), for which the Ångström exponent increases in presence of giant aerosols between 16 and 22%. For the same wavelengths pair than before, it went from 1.39 to 1.61 (+0.22). Finally, for the most stable atmospheric condition (Stab. 3), the absolute difference with respect to the other meteorological conditions is the smallest, with the changes in the Ångström exponent ranging from −0.09 (−7%) to 0.01 (+1%).

 doi:10.20944/preprints202411.1884.v1

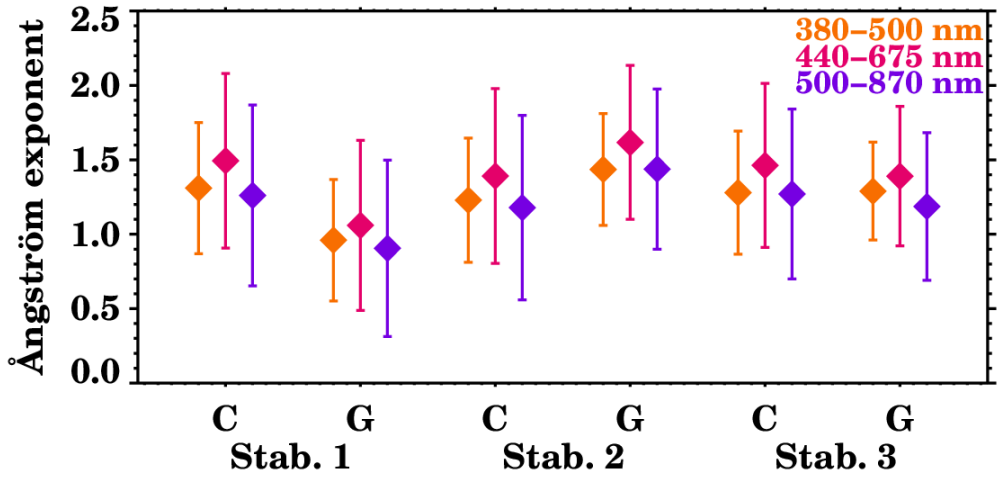

Figure 13. Mean Ångström exponent values during control and giant aerosol cases according to the atmospheric stability for three wavelength pairs: 380 − 500 nm, 440 − 675 nm and 500 − 870 nm. The error bars correspond to the standard deviation. "C" stands for control cases, "G" for giant aerosols observations, and "Stab." for atmospheric stability condition, where "1" has the lower stability and "3" the highest.

Table 4. Mean Ångström exponent values during control and giant aerosol cases according to the atmospheric stability, where "1" has the lower stability and "3" the highest. The values after the ± sign correspond to the standard deviation.

Wavelength pair [nm]	Stability condition 1		Stability condition 2		Stability condition 3	
	Control	Giant	Control	Giant	Control	Giant
380 – 500	1.32 ± 0.43	0.95 ± 0.43	1.22 ± 0.42	1.44 ± 0.36	1.28 ± 0.41	1.29 ± 0.33
440 – 675	1.50 ± 0.59	1.06 ± 0.57	1.39 ± 0.60	1.61 ± 0.52	1.46 ± 0.55	1.39 ± 0.47
500 – 870	1.27 ± 0.60	0.93 ± 0.57	1.18 ± 0.61	1.44 ± 0.54	1.29 ± 0.55	1.20 ± 0.48

The Ångström exponent gives a rough indication of the particle size: lower values indicate the presence of big particles, and higher values of smaller particles. Accordingly, during giant aerosols cloud radar observations, the sun photometer measured coarser particles in low atmospheric stability conditions, finer in neutral conditions and particles roughly of the same size for stable atmospheric conditions. Since the sun photometer measurements are columnar and cover a broad range of the aerosol size spectrum, the changes in Ångström exponent can be attributed to major or minor fraction, and thus presence, of coarse aerosol particles. For Condition 1, the travelled path of desert dust particles prior to reaching the site (see Figure 12) is the shortest, and therefore a smaller fraction of the coarse mode is removed due to gravitational settling. For Condition 3, instead, the dust particles reach the observational site after travelling through a longer path, and most of the big particles could have been removed from the atmosphere in the meantime. Furthermore, the presence of marine particles cannot be neglected for none of these conditions, and aerosols belonging to Condition 3 might also contain continental pollution due to the air masses trajectories.

3.2.3. Accumulated Precipitation

In this section, we performed an inferential analysis to assess how the presence of giant particles affects the accumulated precipitation, given that giant aerosols can act as GCCN and IN, affecting the precipitation formation and the temperature at which ice nucleation initiates. Hence, the giant aerosol together with the aerosol-giant-free observations are compared to precipitation measurements, in order to investigate the effect on the accumulated precipitation.

 doi:10.20944/preprints202411.1884.v1

The analysis is performed at a regional scale, assuming that lofted aerosol layers can be considered homogeneous within a range of $\leq$ 100 *km* and 10 *hours*. The selected criteria follow the adopted strategy by Pappalardo *et al.* [55] for correlative EARLINET-CALIPSO measurements. That study found that in a range of $\leq$ 100 *km*, for aerosol layers in the free troposphere, above 2 *km* of altitude, the mean differences profiles do not change significantly with the time shifts that they considered (between 10 and 720 *min*). The precipitation measurements that we used are performed by the Basilicata Regional Civil Protection: its rain gauges network comprises 46 stations, which are distributed into eight hydrological basins [56] and are a maximum of 100 *km* away from our observational site.

Table 5 presents the mean precipitation accumulation during 6, 12, 18 and 24 *h* after giant aerosols and control observations. The minimum time interval was chosen considering wind speed data and the distance ($\sim$ 10 *km*) of the furthest of the network's rain gauge. Pappalardo *et al.* [55] reported that the typical wind speed in the free troposphere at EARLINET stations ranged between 5 and 20 m/s. The rest of the time intervals are 6 *h* steps so as to facilitate the inferential analysis.

The mean accumulated rain following the event was found to be higher after giant aerosol observations for all the atmospheric stability conditions and for all the time intervals with only one exception: a decrease is registered for Condition 2 for the longest time period. The biggest increase in accumulated precipitation was registered for Condition 1 during the 12 *h* following the giant aerosols observations, and it was of 18.8 *mm* (from 1.3 to 20.1 *mm*). In relative difference, though, the highest increase occurred, also for Condition 1, during the 6 *h* after the event: the accumulated precipitation went from 0.7 to 14.4 *mm*, almost 20 times higher. Among all the time intervals, the lowest accumulated rain increase was detected for Condition 2 (intermediate atmospheric stability).

For the 6 *h* time interval, the highest increase corresponds to Condition 1 (13.7 *mm*). For the 12 *h* period, the maximum increase was registered for Condition 1 as well, and corresponds to a relative increase in respect to the control of 1446%. For the 18 and 24 *h* time intervals, the relative increases were lower: 142% after 18 *h* (Condition 1) and 50% after 24 *h* (Condition 3), but given the time scales for these longer time intervals, it is difficult to attribute the effect on the presence of giant particles.

Table 5. Mean precipitation accumulation in *mm* during the 6, 12, 18 and 24 *hours* after giant aerosols and control observations according to the atmospheric stability conditions, where "1" has the lower stability and "3" the highest. The values after the $\pm$ sign correspond to the standard deviation.

Time interval [*h*]	Stability condition 1		Stability condition 2		Stability condition 3	
	Control	Giant	Control	Giant	Control	Giant
6	0.7 ± 2.7	14.4 ± 50.2	0.9 ± 1.9	4.1 ± 13.6	1.0 ± 2.4	10.8 ± 19.4
12	1.3 ± 3.1	20.1 ± 70.6	1.0 ± 2.5	4.4 ± 13.7	3.0 ± 17.0	12.0 ± 20.3
18	12.1 ± 57.2	29.7 ± 85.9	3.7 ± 17.4	9.3 ± 27.6	8.4 ± 33.3	13.9 ± 20.4
24	31.6 ± 113	38.9 ± 119.1	14.1 ± 45.7	11.7 ± 38.4	10.1 ± 39.4	17.0 ± 23.3

4. Summary and Conclusions

This work intended to fill the observational gap in the characterization of the aerosol size distribution in the region of the giant and ultragiant fraction by using a Ka-band cloud radar (8.45 *mm* wavelength) and to get a deeper understanding of their characteristics and their effects on some atmospheric variables, both at a local and at a regional scale.

With this purpose, a novel methodology for giant and ultragiant aerosols detection was developed, which enabled the systematic classification of observations and characterization of giant aerosols using cloud radar measurements. In summary, this new methodology consists in separating the cloud radar observations of non-hydrometeor targets into aerosols and insects, for which the findings of several entomology studies regarding the insects behaviour in the atmosphere were used. The application of the methodology to approximately six years of measurements (March 2009 – June 2015) yielded to the identification of more than three hundred giant aerosol layers. The maximum number of layers

 doi:10.20944/preprints202411.1884.v1

observed occurred during summer, and a relative maximum was observed in spring. Together with a minimum during winter, the seasonal evolution of giant aerosols is in agreement with climatological studies of the site realized using lidar measurements [i.e. 53]. Lastly, considering the continuous cloud radar operation, the developed methodology could be very useful for monitoring in near real-time the coarse aerosol fraction of aerosol particles such as dust, pollen and volcanic aerosols.

After the systematic identification of giant aerosols in cloud radar measurements, their effects on the local meteorology were studied by correlating the observations of giant particles with three atmospheric variables and comparing them to control observations (cases in which giant particles were not observed). The approach followed in this investigation is based on the selection of a day-time interval and the screening of the data according to the atmospheric stability, which was estimated by the pressure vertical velocity in the upper atmosphere.

Giant aerosols were found to cause an Aerosol Optical Depth (AOD) increase, which ranged from 6% to 90% in respect to the control cases, contributing to an increase of the aerosol load for all the atmospheric stability conditions.

The Ångström exponent was also affected by giant aerosols: it decreased for the highest and lowest atmospheric stability and it increased for the intermediate stability conditions. This means that coarser aerosols were observed for the most extreme conditions and finer particles were observed for the intermediate situation. The decrease ranged between 5% and 43%, while the increase ranged between 17% and 22%. Considering that the AOD and Ångström exponent measurements are columnar, this suggests that giant aerosols represent an important fraction of the columnar aerosol load.

Finally, an increase of the accumulated precipitation was found after the observations of giant aerosols. This increase was found for all time intervals, and more significantly for the most unstable atmospheric conditions, which expectedly favours convection processes. These results are in line with findings from other studies, such as Eagan *et al.* [6] and Feingold *et al.* [5], who found that GCCN concentration of $10^{-3}\ cm^{-3}$ is enough to increase the amount of rain in stratocumuli by up to 100%, Jung *et al.* [12], where they artificially introduced GCCN into stratocumulus clouds and found an increase in the average drizzle rates during the $30 - 60$ *minutes* after the seeding, and Liu *et al.* [57], where they found that the raindrop size, concentration and rain rate increased in the presence of coarse sea spray aerosols. Given that precipitation can be affected by several factors and conditions as well as the uncertainties of our analysis, this study suggests that giant particles may have a role in precipitation and calls for further research.

In conclusion, we found that giant aerosols had an effect on the AOD, the Ångström exponent and the accumulated precipitation. Nevertheless, the standard deviations associated with the variables indicate high variability, and considering that these variables can be affected by a number of parameters, this study highlights a role of giant aerosols on the regional and local meteorology, but does not allow to fully disentangle their effect. Thus, we need to expand our dataset with a longer data record in order to vigorously assess the effects on the different meteorological variables and draw accurate conclusions. This could be done by categorizing the cases according to the aerosol type (i.e. dust/marine/pollen), by associating them to the cloud type formation (i.e. cumuli vs stratocumuli), or by assessing the different atmospheric variables' seasonality.

Although uncertainties remain, the importance and utility of the proposed methodology is supported by our preliminary findings, and the impact that the giant aerosols can have on some meteorological variables is displayed.

Author Contributions: Conceptualization, P.G-C., F.M. and A.A.; methodology, P.G-C.; software, P.G-C.; validation, F.M., A.A., M.B-P. and N.P.; resources, G.P.; writing—original draft preparation, P.G-C.; writing—review and editing, F.M., A.A., N.P., M.B-P. and M.R.; visualization, P.G-C.; supervision, F.M., A.A. and M.B-P.; project administration, A.A.; funding acquisition, G.P. All authors have read and agreed to the published version of the manuscript.

Funding: This research was funded by the European Community through the ACTRIS Research Infrastructure Action under the 7^{th} Framework Programme under ACTRIS Grant Agreement n° 262254 and ITaRS Grant Agreement n° 289923, by the Italian national project "Programma Operativo Nazionale (PON) Regione Basilicata

 doi:10.20944/preprints202411.1884.v1

2000/2006", and by IR0000032—ITINERIS, Italian Integrated Environmental Research Infrastructures System (D.D. no. 130/2022—CUP B53C22002150006), funded by the EU—Next Generation EU PNRR-Mission 4 "Education and Research"—Component 2: "From research to business"—Investment 3.1: "Fund for the realization of an integrated system of research and innovation infrastructures"..

Data Availability Statement: The MIRA36 Ka-band Doppler radar data and the ECMWF NWP model outputs can be accessed in the CLOUDNET website (https://cloudnet.fmi.fi/search/data?site=potenza), whilst the sun photometer (CE-318) data can be found in the AERONET website (https://aeronet.gsfc.nasa.gov/cgi-bin/draw_map_display_aod_v3?level=3). The data from the MWR (MP3010), the MILOS weather station and the ceilometer (CT25K) are stored at the CIAO facilities, and can be made available upon request.

Conflicts of Interest: "The authors declare no conflicts of interest." "The funders had no role in the design of the study; in the collection, analyses, or interpretation of data; in the writing of the manuscript; or in the decision to publish the results".

Abbreviations

The following abbreviations are used in this manuscript:

ABL	Atmospheric Boundary Layer
AERONET	Aerosol Robotic Network
AOD	Aerosol Optical Depth
BT	Brightness Temperature
CCN	Cloud Condensation Nuclei
CIAO	CNR-IMAA Atmospheric Observatory
COD	Cloud Optical Depth
ECMWF	European Centre for Medium-Range Weather Forecasts
GCCN	Giant Cloud Condensation Nuclei
IN	Ice Nuclei
IWP	Integrated Water Vapour
LDR	Linear Depolarization Ratio
LT	Local Time
LWP	Liquid Water Path
MWR	Microwave Radiometer
NWP	Numerical Weather Prediction
R	Rain Rate
RMS	Peak Width
SNR	Signal-to-Noise Ratio
VEL	Doppler Velocity
Z	Equivalent Reflectivity

References

1. Pöschl, U. Atmospheric Aerosols: Composition, Transformation, Climate and Health Effects. *Angewandte Chemie International Edition* **2005**, *44*, 7520–7540. doi:10.1002/anie.200501122.
2. Pappalardo, G.; Mona, L.; D'Amico, G.; Wandinger, U.; Adam, M.; Amodeo, A.; Ansmann, A.; Apituley, A.; Alados Arboledas, L.; Balis, D.; Boselli, A.; Bravo-Aranda, J.A.; Chaikovsky, A.; Comeron, A.; Cuesta, J.; De Tomasi, F.; Freudenthaler, V.; Gausa, M.; Giannakaki, E.; Giehl, H.; Giunta, A.; Grigorov, I.; Groß, S.; Haeffelin, M.; Hiebsch, A.; Iarlori, M.; Lange, D.; Linné, H.; Madonna, F.; Mattis, I.; Mamouri, R.E.; McAuliffe, M.A.P.; Mitev, V.; Molero, F.; Navas-Guzman, F.; Nicolae, D.; Papayannis, A.; Perrone, M.R.; Pietras, C.; Pietruczuk, A.; Pisani, G.; Preißler, J.; Pujadas, M.; Rizi, V.; Ruth, A.A.; Schmidt, J.; Schnell, F.; Seifert, P.; Serikov, I.; Sicard, M.; Simeonov, V.; Spinelli, N.; Stebel, K.; Tesche, M.; Trickl, T.; Wang, X.; Wagner, F.; Wiegner, M.; Wilson, K.M. Four-dimensional distribution of the 2010 Eyjafjallajökull volcanic cloud over Europe observed by EARLINET. *Atmospheric Chemistry and Physics* **2013**, *13*, 4429–4450. doi:10.5194/acp-13-4429-2013.
3. Rosenfeld, D.; Andreae, M.O.; Asmi, A.; Chin, M.; de Leeuw, G.; Donovan, D.P.; Kahn, R.; Kinne, S.; Kivekäs, N.; Kulmala, M.; Lau, W.; Schmidt, K.S.; Suni, T.; Wagner, T.; Wild, M.; Quaas, J. Global observations of aerosol-cloud-precipitation-climate interactions. *Reviews of Geophysics* **2014**, *52*, 750–808,

 doi:10.20944/preprints202411.1884.v1

[https://agupubs.onlinelibrary.wiley.com/doi/pdf/10.1002/2013RG000441]. https://doi.org/10.1002/2013RG000441.

4. Dagan, G.; Koren, I.; Altaratz, O. Aerosol effects on the timing of warm rain processes. *Geophysical Research Letters* **2015**, pp. n/a–n/a. doi:10.1002/2015GL063839.
5. Feingold, G.; Cotton, W.; Kreidenweis, S.; Davis, J. The Impact of Giant Cloud Condensation on Drizzle Formation in Stratocumulus: Implications for Cloud Radiative Properties. *J. Atmos. Sci.* **1999**, *56*, 4100–4117.
6. Eagan, R.; Hobbs, P.; Radke, L. Measurements of CCN and cloud droplet size distribution in the vicinity of forest fires. *J. Appl. Meteor.* **1974**, *13*, 553–537.
7. DeMott, P.J.; Sassen, K.; Poellot, M.R.; Baumgardner, D.; Rogers, D.C.; Brooks, S.D.; Prenni, A.J.; Kreidenweis, S.M. African dust aerosols as atmospheric ice nuclei. *Geophysical Research Letters* **2003**, *30*, n/a–n/a. doi:10.1029/2003GL017410.
8. Möhler, O.; Field, P.R.; Connolly, P.; Benz, S.; Saathoff, H.; Schnaiter, M.; Wagner, R.; Cotton, R.; Krämer, M.; Mangold, A.; Heymsfield, A.J. Efficiency of the deposition mode ice nucleation on mineral dust particles. *Atmospheric Chemistry and Physics* **2006**, *6*, 3007–3021. doi:10.5194/acp-6-3007-2006.
9. Ghate, V.P.; Albrecht, B.A.; Kollias, P.; Jonsson, H.H.; Breed, D.W. Cloud seeding as a technique for studying aerosol-cloud interactions in marine stratocumulus. *Geophysical Research Letters* **2007**, *34*, [https://agupubs.onlinelibrary.wiley.com/doi/pdf/10.1029/2007GL029748]. https://doi.org/10.1029/2007GL029748.
10. Jung, E.; Albrecht, B.A.; Feingold, G.; Jonsson, H.H.; Chuang, P.; Donaher, S.L. Aerosols, clouds, and precipitation in the North Atlantic trades observed during the Barbados aerosol cloud experiment – Part 1: Distributions and variability. *Atmospheric Chemistry and Physics* **2016**, *16*, 8643–8666. doi:10.5194/acp-16-8643-2016.
11. Segal, Y.; Khain, A.; Pinsky, M.; Rosenfeld, D. Effects of hygroscopic seeding on raindrop formation as seen from simulations using a 2000-bin spectral cloud parcel model. *Atmospheric Research* **2004**, *71*, 3–34. Weather Modification, doi:https://doi.org/10.1016/j.atmosres.2004.03.003.
12. Jung, E.; Albrecht, B.A.; Jonsson, H.H.; Chen, Y.C.; Seinfeld, J.H.; Sorooshian, A.; Metcalf, A.R.; Song, S.; Fang, M.; Russell, L.M. Precipitation effects of giant cloud condensation nuclei artificially introduced into stratocumulus clouds. *Atmospheric Chemistry and Physics* **2015**, *15*, 5645–5658. doi:10.5194/acp-15-5645-2015.
13. Khain, A.; Ovchinnikov, M.; Pinsky, M.; Pokrovsky, A.; Krugliak, H. Notes on the state-of-the-art numerical modeling cloud microphysics. *Atmospheric Research* **2000**, *55*, 159–224. doi:10.1016/S0169-8095(00)00064-8.
14. Reiche, C.; Lasher-Trapp, S. The minor importance of giant aerosol to precipitation development within small trade wind cumuli observed during RICO. *Atmospheric Research - ATMOS RES* **2010**, *95*, 386–399. doi:10.1016/j.atmosres.2009.11.002.
15. Minor, H.; Rauber, R.; Göke, S.; Girolamo, L. Trade Wind Cloud Evolution Observed by Polarization Radar: Relationship to Giant Condensation Nuclei Concentrations and Cloud Organization. *Journal of The Atmospheric Sciences - J ATMOS SCI* **2011**, *68*, 1075–1096. doi:10.1175/2010JAS3675.1.
16. Di Girolamo, P.; De Rosa, B.; Summa, D.; Franco, N.; Veselovskii, I. Measurements of Aerosol Size and Microphysical Properties: A Comparison Between Raman Lidar and Airborne Sensors. *Journal of Geophysical Research: Atmospheres* **2022**, *127*, e2021JD036086, [https://agupubs.onlinelibrary.wiley.com/doi/pdf/10.1029/2021JD036086]. e2021JD036086 2021JD036086, doi:https://doi.org/10.1029/2021JD036086.
17. Mamouri, R.E.; Ansmann, A. Potential of polarization lidar to provide profiles of CCN- and INP-relevant aerosol parameters. *Atmospheric Chemistry and Physics* **2016**, *16*, 5905–5931. doi:10.5194/acp-16-5905-2016.
18. van der Does, M.; Knippertz, P.; Zschenderlein, P.; Harrison, R.G.; Stuut, J.B.W. The mysterious long-range transport of giant mineral dust particles. *Science Advances* **2018**, *4*, eaau2768, [https://www.science.org/doi/pdf/10.1126/sciadv.aau2768]. doi:10.1126/sciadv.aau2768.
19. Middleton, N.; Betzer, P.; Bull, P. Long-range transport of 'giant' aeolian quartz grains: linkage with discrete sedimentary sources and implications for protective particle transfer. *Marine Geology* **2001**, *177*, 411–417. doi:https://doi.org/10.1016/S0025-3227(01)00171-2.
20. Ryder, C.L.; Highwood, E.J.; Rosenberg, P.D.; Trembath, J.; Brooke, J.K.; Bart, M.; Dean, A.; Crosier, J.; Dorsey, J.; Brindley, H.; others. Optical properties of Saharan dust aerosol and contribution from the coarse mode as measured during the Fennec 2011 aircraft campaign. *Atmospheric Chemistry and Physics* **2013**, *13*, 303–325.
21. Ginoux, P.; Prospero, J.; Gill, T.; Hsu, N. Natural and anthropogenic dust: From sources to radiative forcing derived from satellite data and GFDL climate model. *Proceedings of the Fall Meeting, American Geophysical Union* **2011**.

22. Madonna, F.; Amodeo, A.; D'Amico, G.; Mona, L.; Pappalardo, G. Observation of non-spherical ultragiant aerosol using a microwave radar. *Geophys. Res. Lett.* **2010**, *37*. doi:10.1029/2010GL044999.
23. Madonna, F.; Amodeo, A.; D'Amico, G.; Pappalardo, G. A study on the use of radar and lidar for characterizing ultragiant aerosol. *Geophys. Res.* **2013**, *118*. doi:10.1002/jgrd.50789.
24. Madonna, F.; Amodeo, A.; Boselli, A.; Cornacchia, C.; Cuomo, V.; D'Amico, G.; Giunta, A.; Mona, L.; Pappalardo, G. CIAO: the CNR-IMAA advanced observatory for atmospheric research. *Atmos. Meas. Tech.* **2011**, *4*, 1191–1208.
25. Mona, L.; Papagiannopoulos, N.; Basart, S.; Baldasano, J.; Binietoglou, I.; Cornacchia, C.; Pappalardo, G. EARLINET dust observations vs. BSC-DREAM8b modeled profiles: 12-year-long systematic comparison at Potenza, Italy. *Atmospheric Chemistry and Physics* **2014**, *14*, 8781–8793. doi:10.5194/acp-14-8781-2014.
26. Pappalardo, G.; Amodeo, A.; Mona, L.; Pandolfi, M.; Pergola, N.; Cuomo, V. Raman lidar observations of aerosol emitted during the 2002 Etna eruption. *Geophys. Res. Lett.* **2004**, *31*. doi:10.1029/2003GL019073.
27. Mishchenko, M.I.; Travis, L.D.; Mackowski, D.W. T-matrix computations of light scattering by nonspherical particles: A review. *Journal of Quantitative Spectroscopy and Radiative Transfer* **1996**, *55*, 535–575. Light Scattering by Non-Spherical Particles, doi:10.1016/0022-4073(96)00002-7.
28. Zhang, Y.; Saito, M.; Yang, P.; Schuster, G.; Trepte, C. Sensitivities of Spectral Optical Properties of Dust Aerosols to Their Mineralogical and Microphysical Properties. *Journal of Geophysical Research: Atmospheres* **2024**, *129*, e2023JD040181, [https://agupubs.onlinelibrary.wiley.com/doi/pdf/10.1029/2023JD040181]. e2023 JD040181 2023JD040181, doi:https://doi.org/10.1029/2023JD040181.
29. Weinzierl, B.; Sauer, D.; Minikin, A.; Reitebuch, O.; Dahlkötter, F.; Mayer, B.; Emde, C.; Tegen, I.; Gasteiger, J.; Petzold, A.; Lambert, A.; Kueppers, U.; Schumann, U. On the visibility of airborne volcanic ash and mineral dust from the pilot's perspective in flight. *J. Phys. Chem. Earth.* **2012**, *45-46*, submitted. doi:10.1016/j.pce.2012.04.003.
30. Adams, R.; Perger, F.; Rose, W.; Kostinski, A. Measurements of the complex dielectric constant of volcanic ash from 4 to 19 GHz. *J. Geophys. Res.* **1996**, *101*, 8175–8185.
31. Exton, H.J.; Latham, J.; Park, P.M.; Smith, M.H.; Allan, R.R., The Production and Dispersal of Maritime Aerosol. In *Oceanic Whitecaps: And Their Role in Air-Sea Exchange Processes*; Monahan, E.C.; Niocaill, G.M., Eds.; Springer Netherlands: Dordrecht, 1986; pp. 175–193. doi:10.1007/978-94-009-4668-2_17.
32. Clothiaux, E.; Ackerman, T.; Mace, G.; Moran, K.; Marchand, R.; Miller, M.; Martner, B. Objective determination of cloud heights and radar reflectivities using a combination of active remote sensors at the ARM CART sites. *J. Appl. Meteor.* **2000**, *39*, 645–665.
33. Khandwalla, A.; Majurec, N.; Sekelsky, S.; Williams, C.; Gage, K. Characterization of radar boundary layer data collected during the 2001 multi-frequency radar IOP. *Proceedings of the 12th ARM Science Team Meeting* **2002**.
34. Chapman, J.; Drake, V.; Reynolds, D. Recent insights from radar studies of insect flight. *Annu. Rev. Entomol.* **2011**, *56*, 337–356. doi:10.1146/annurev-ento-120709-144820.
35. Marzano, F.; Barbieri, S.; Vulpiani, G.; Rose, W. Volcanic cloud retrieval by ground-based microwave weather radar. *IEEE Trans. Geosci. Rem. Sens.* **2006**, *44*, 3235–3246.
36. Marzano, F.; Vulpiani, G.; Rose, W. Microphysical Characterization of Microwave Radar Reflectivity Due to Volcanic Ash Clouds. *IEEE Trans. Geosci. and Rem. Sens.* **2006**, *44*, 313–327.
37. Chapman, J.; Reynolds, D.; Smith, A. Vertical-looking radar: a new tool for monitoring high-altitude insect migration. *BioScience* **2004**, *53*, 503–5011.
38. Reynolds, D.; Chapman, J.; Edwards, A.; Smith, A.; Wood, C.; Barlow, J.; Woiwod, I. Radar studies of the vertical distribution of insects migrating over southern Britain: the influence of temperature inversions on nocturnal layer concentrations. *Bull. Entomol. Res.* **2005**, *95*, 259–274.
39. Reynolds, D.; Smith, A.; Chapman, J. A radar study of emigratory flight and layer formation at dawn over southern Britain. *Bull. Entomol. Res.* **2008**, *98*, 35–52.
40. Wood, C.; Chapman, J.; Reynolds, D.; Barlow, J.; Smith, A.; Woiwod, I. The influence of the atmospheric boundary layer on nocturnal layers of moths migrating over southern Britain. *Int. J. Biometeorol.* **2006**, *50*, 193–204.
41. Wood, C.; Reynolds, D.; Wells, P.; Barlow, J.; Woiwod, I.; J.W., C. Flight periodicity and the vertical distribution of high-altitude moth migration over southern Britain. *Bull. Entomol. Res.* **2009**, *99*, 525–535.

42. Drake, V. The vertical distribution of macroinsects migrating in the nocturnal boundary layer: a radar study. *Bound.Layer Meteorol.* **1984**, *28*, 353–374.
43. Drake, V.; Farrow, R. The influence of atmospheric structure and motions on insect migration. *Annu. Rev. Entomol.* **1988**, *33*, 183–210.
44. Gatehouse, A. Behavior and ecological genetics of wind-born migration by insects. *Annu. Rev. Entomol.* **1997**, *42*, 475–502.
45. Reynolds, A.; Reynolds, D.; Riley, J. Does a 'turbophoretic' effect account for layer concentrations of insects migrating in the stable night-time atmosphere? *J. R. Soc. interface* **2009**, *6*, 87–95.
46. Bauer-Pfundstein, M.; Görsdorf, U. Target separation and classification using cloud radar Doppler-spectra. Proceedings 33rd Intern. Conf. on Radar Meteorology, Cairns, 2007.
47. Luke, E.; Kollias, P.; K.L., J. A technique for the automatic detection of insect clutter in cloud radar returns. *J. Atmos. Ocean. Techn.* **2007**, *25*, 1498–1513.
48. Møller, A. Long-term trends in wind speed, insect abundance and ecology of an insectivorous bird. *Ecosphere* **2013**, *4*. doi:10.1890/ES12-00310.1.
49. Reid, D.; Wardhaugh, K.; Roffey, J. Radar studies of insect flight at Benalla, Victoria, in February 1974. *CSIRO Aust. Div. Entomol. Tech. Pap.* **1979**, *16*, 21.
50. Wood, C.; O'Connor, E.; Hurley, R.; Reynolds, D.; Illingworth, A. Cloud-radar observations of insects in the UK convective boundary layer. *Meteorol. Appl.* **2009**, *16*, 491–500.
51. Liu, L.; Mishchenko, M.I. Spectrally dependent linear depolarization and lidar ratios for nonspherical smoke aerosols. *Journal of Quantitative Spectroscopy and Radiative Transfer* **2020**, *248*, 106953.
52. Mona, L.; Amodeo, A.; Pandolfi, M.; Pappalardo, G. Saharan dust intrusions in the Mediterranean area: Three years of Raman lidar measurements. *Journal of Geophysical Research: Atmospheres (1984–2012)* **2006**, *111*.
53. Mona, L.; Pappalardo, G.; Amodeo, A.; d'Amico, G.; Madonna, F.; Boselli, A.; Giunta, A.; Russo, F.; Cuomo, V. One year of CNR-IMAA multi-wavelength Raman lidar measurements in coincidence with CALIPSO overpasses: Level 1 products comparison. *Atmospheric Chemistry and Physics* **2009**, *9*, 7213–7228.
54. Koren, I.; Altaratz, O.; Remer, L.A.; Feingold, G.; Martins, J.V.; Heiblum, R.H. Aerosol-induced intensification of rain from the tropics to the mid-latitudes. *Nature Geoscience* **2012**, *5*, 118–122.
55. Pappalardo, G.; Wandinger, U.; Mona, L.; Hiebsch, A.; Mattis, I.; Amodeo, A.; Ansmann, A.; Seifert, P.; Linné, H.; Apituley, A.; Alados Arboledas, L.; Balis, D.; Chaikovsky, A.; D'Amico, G.; De Tomasi, F.; Freudenthaler, V.; Giannakaki, E.; Giunta, A.; Grigorov, I.; Iarlori, M.; Madonna, F.; Mamouri, R.E.; Nasti, L.; Papayannis, A.; Pietruczuk, A.; Pujadas, M.; Rizi, V.; Rocadenbosch, F.; Russo, F.; Schnell, F.; Spinelli, N.; Wang, X.; Wiegner, M. EARLINET correlative measurements for CALIPSO: First intercomparison results. *Journal of Geophysical Research: Atmospheres* **2010**, *115*, [https://agupubs.onlinelibrary.wiley.com/doi/pdf/10.1029/2009JD012147]. doi:https://doi.org/10.1029/2009JD012147.
56. Centro Funzionale Decentrato, P.C.R.B. Mappa stazioni, 2024. https://centrofunzionale.regione.basilicata.it/ [Last accessed: 19/11/2024].
57. Liu, F.; Rosenfeld, D.; Pan, Z.; Zang, L.; F., M. Combined effects of fine and coarse marine aerosol on vertical raindrop size distribution. *npj Climate and Atmospheric Science* **2024**, *7*, 2397–3722. doi:https://doi.org/10.1038/s41612-024-00730-1.